New Journal of Physics
The open access journal at the forefront of physics

Deutsche Physikalische Gesellschaft DPG
IOP Institute of Physics

Published in partnership with: Deutsche Physikalische Gesellschaft and the Institute of Physics

OPEN ACCESS

RECEIVED
21 September 2018

REVISED
4 February 2019

ACCEPTED FOR PUBLICATION
20 March 2019

PUBLISHED
30 April 2019

PAPER

On the performance of an ENZ-based sensor using transmission line theory and effective medium approach

V Pacheco-Peña[1,2,5], **M Beruete**[3,4,5], **P Rodríguez-Ulibarri**[3] and **N Engheta**[2,5]

[1] Emerging Technologies and Materials group, School of Engineering, Newcastle University, Newcastle Upon Tyne, NE17RU, United Kingdom
[2] Department of Electrical and Systems Engineering, University of Pennsylvania, Philadelphia, PA 19104, United States of America
[3] Antennas Group-TERALAB, Universidad Pública de Navarra, Campus Arrosadía, SE-31006 Pamplona, Spain
[4] Institute of Smart Cities, Universidad Pública de Navarra, SE-31006, Pamplona, Spain
[5] Authors to whom any correspondence should be addressed.

E-mail: victor.pacheco-pena@newcastle.ac.uk, miguel.beruete@unavarra.es, pablo.rodriguez@unavarra.es and engheta@ee.upenn.edu

Keywords: epsilon-near-zero, metamaterials, sensing, metamaterial sensor, subwavelength sensing

Abstract

In this paper we perform an in-depth theoretical study of a sensing platform based on epsilon-near-zero (ENZ) metamaterials. The structure proposed for sensing is a narrow metallic waveguide channel. An equivalent circuit model is rigorously deduced using transmission line theory, considering several configurations for a dielectric body (analyte sample) inserted within the narrow channel, showing good agreement with results obtained from numerical simulations. The transmission line model is able to reproduce even the most peculiar details of the sensing platform response. Its performance is then evaluated by varying systematically the size, position and permittivity of the analyte, and height of the ENZ channel. It is shown that the sensor is capable of detecting changes in the permittivity/refractive index or position even with deeply subwavelength analyte sizes ($\sim 0.05\lambda_0$), giving a sensitivity up to 0.03 m/RIU and a figure of Merit ~25. The effective medium approach is evaluated by treating the inhomogeneous cross-section of the analyte as a transmission line filled with a homogeneous material.

1. Introduction

Since metamaterials were introduced several years ago, the possibility to arbitrarily control the electromagnetic parameters of a material has become a strong field of research in the scientific community [1]. Owing to the small size of the constituent unit cells of metamaterials (when compared to the operating wavelength), some aspects of effective medium theory can be utilized to describe the electromagnetic wave propagation inside them. Metamaterials research has opened the door towards the design of artificial media with exotic values of permittivity (ε) and permeability (μ) by properly engineering the geometry, materials and arrangement of the unit cells [2–21].

Within this context, metamaterials with near-zero values of permittivity, so called epsilon-near-zero (ENZ) metamaterials, have become an interesting subfield of research due to their fascinating properties, such as an almost infinite wavelength and close to zero values of group velocity in unbounded lossless ENZ media (note that in most cases when we have a finite region of ENZ and some loss, the group velocity is not near zero, although it is always less than the velocity of light in vacuum) [22, 23]. Also the propagation constant is close to zero which implies a near-zero phase delay of the waves propagating inside these media. These peculiar properties have opened the way to explore fascinating features such as squeezing, supercoupling and tunneling of electromagnetic waves [24–26], which were first reported theoretically in [23, 24] and experimentally demonstrated at microwave frequencies [27, 28]. Recently, they have also been demonstrated at the near infrared and visible frequencies by using metal-dielectric-metal multilayers [29–31].

Inspired by the recent development in ENZ metamaterials, several applications have been reported including nanocircuits [32, 33], nonlinear control [34], impedance matched coaxial to waveguide transitions [35], antennas [36–38], levitation of particles [39], Fourier transformation [40], and beam shaping [41–45], to name a few, demonstrating that this type of metamaterial can be utilized in a variety of applications and frequency ranges. It is important to highlight that some of these applications have been developed by simply using the structural dispersion of a narrow hollow rectangular waveguide working near the cutoff of the fundamental TE_{10} mode in order to emulate an ENZ medium, as it was used several decades ago to emulate plasmas at microwave frequencies using parallel-plate waveguides [46]. Hence, inspired by this concept, ENZ metamaterials for sensing applications have been recently proposed using a narrow hollow waveguide channel connected in between two waveguides and placing a particle in the middle of the ENZ channel [47].

In the present work, we build upon the work reported in [47] and extend it into the general case when the analyte (i.e. a dielectric particle under test) fills partially the channel in the transversal x dimension. In section 2, the transmission line model is utilized and explained and the general expressions for the transmission coefficient are deduced. Then, in section 3, the transmission properties along with an in-depth explanation of the most relevant features are discussed for different scenarios: a dielectric cuboid in the middle of the channel, a dielectric slab filling completely the narrow channel along the propagation direction, and a dielectric slab filling completely the narrow channel along the transversal axis (this is the case analyzed in [47], and is considered here as a special example of our generalized approach). The sensor performance in terms of sensitivity and figure of merit (FOM) is characterized for the dielectric cuboid case. Moreover, the advantages of dielectric sensing under ENZ operation are also discussed. In particular, it is shown that the response of the sensor is more robust at this frequency in terms of frequency shift versus analyte position as compared with the next transmission peak due to the half-wavelength Fabry–Perot (FP) resonance. Also, an effective medium approach is proposed to treat the cross-section containing the analyte as a transmission line section filled with a slab with an effective permittivity. Several configurations of the analyte are then evaluated using this approach, demonstrating the advantage of using this powerful tool. All the results here presented are compared to numerical simulations using the commercial software CST Microwave Studio®, and good agreement is obtained. Section 4 summarizes the main conclusions.

2. General geometry of the sensor and equivalent transmission line

In this section, the general expressions of the transmission coefficient are derived using the transmission line model. A schematic representation of the sensor used is shown in figure 1(a). It consists of a narrow ENZ channel of length L filled with air (colored in blue) surrounded by two waveguides filled with a dielectric of relative permittivity ε_{wg} (colored in green). The width of all elements is $b = \lambda_0/2$, where λ_0 is the cutoff wavelength of the narrow channel filled with air. The height of the input and output waveguides is $a = b/2$ and that of the ENZ channel is $a_{\mathrm{ENZ}} = a\Delta_a$, where Δ_a is a factor between 0 and 1. The ENZ channel has a U-shape, following the same procedure as in [25, 47], and the vertical walls have a length along z equal to a_{ENZ}. Finally, a red particle representing the analyte, with dimensions $L_x \times L_z$ and permittivity ε_a is placed inside the ENZ channel at the point $(\Delta_x(b/2 - L_x/2), \Delta_z(L/2 - L_z/2))$, where $|\Delta_x|, |\Delta_z| \in [0, 1]$ so that $|\Delta_x|, |\Delta_z| = 0, 1$ means that the analyte is in the center or at the extremes, respectively. The cross-sections on the xz- and xy- planes of the analyte are also shown as inset in the same figure. Moreover, since a systematic study of the sensing performance for different widths and positions of the analyte will be done in the following sections, the dimensions of each section of the ENZ channel (see figure 1(a)) are defined as follows:

$$L_{ch1,2} = \frac{1}{2}(L - L_z)(1 \mp \Delta_z), \tag{1}$$

$$L_{x1,2} = \frac{1}{2}(b - L_x)(1 \mp \Delta_x), \tag{2}$$

where the minus (plus) sign stands for subindex '1' ('2').

We can now apply the transmission line theory to analyze the response of this structure. The equivalent transmission line problem is shown in figure 1(b). Each section in the figure represents the different parts of the sensor: input and output waveguides (green), vertical walls filled with air (which are responsible for coupling and tunneling the incoming wave inside the narrow ENZ channel [25, 47]) and ENZ channel (blue), and analyte (red). Each element in the network (surrounded by a dashed line) can be described with a transmission ($ABCD$) matrix, so that the overall response is [48]:

$$(ABCD)_{\mathrm{total}} = \begin{bmatrix} A_{\mathrm{total}} & B_{\mathrm{total}} \\ C_{\mathrm{total}} & A_{\mathrm{total}} \end{bmatrix}, \tag{3a}$$

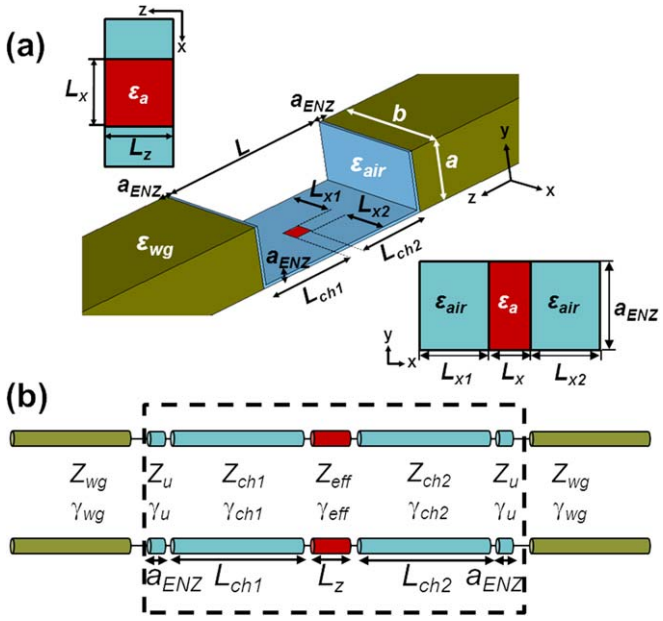

Figure 1. (a) Schematic representation of the ENZ-based sensor consisting of a U shaped narrow channel filled with air and connected in between two waveguides filled with a dielectric with permittivity ε_{wg}. The analyte is placed within the narrow channel and its dimensions are shown in the insets. (b) Equivalent transmission line of the sensor.

$$(ABCD)_{\text{total}} = \prod_i (ABCD)_i = \prod_i \begin{bmatrix} A_i & B_i \\ C_i & A_i \end{bmatrix} = \prod_i \begin{bmatrix} \cosh(-i\gamma_i L_i) & Z_i \sinh(-i\gamma_i L_i) \\ (1/Z_i)\sinh(-i\gamma_i L_i) & \cosh(-i\gamma_i L_i) \end{bmatrix}, \tag{3b}$$

where the subscript i represents each transmission line section with length L_i, propagation constant γ_i, and characteristic impedance Z_i. In general the intrinsic dispersive behavior of a rectangular waveguide can be described with a relative effective permittivity as a Drude model [42, 49] so that the propagation constant can be expressed as:

$$\gamma_i = k_0 \sqrt{\varepsilon_{\text{eff},i}}, \tag{4}$$

where k_0 is the free-space wavenumber, $\varepsilon_{\text{eff},i}$ is the effective permittivity in each section and the time convention $e^{-i\omega t}$ is assumed. If the waveguide is homogeneously filled, the effective permittivity follows a simple equation:

$$\varepsilon_{\text{eff},i} = \varepsilon_i - \left(\frac{\pi}{k_0 b}\right)^2, \tag{5}$$

where ε_i is relative permittivity of the dielectric filling that section. From this expression it is clear that near the waveguide cutoff the effective permittivity is close to zero and we can effectively emulate an ENZ metamaterial. Above cutoff, $\varepsilon_{\text{eff},i} > 0$ and the propagation constant is real ($\gamma_i = \beta_i$) as corresponds to a propagating wave, whereas below cutoff $\varepsilon_{\text{eff},i} < 0$ the propagation constant is imaginary ($\gamma_i = i\alpha_i$) and the wave suffers reactive attenuation (exponential reduction).

If the waveguide is inhomogeneous (as happens when the analyte does not fill completely the cross-section), one should apply a homogenization procedure to calculate the propagation constant, assuming that the waveguide cross-section is completely filled with a block of effective permittivity $\varepsilon_{\text{eff},i}$ (see inset in figure 1(a)). The value of the propagation constant in that section is then obtained following the method discussed in [48] extended here to the three region case shown in figure 1(a). After applying the boundary conditions of vanishing tangent electric field at the metallic walls and the continuity of the tangential components of the electric and magnetic fields at the interfaces between the analyte and air, the next equations are obtained:

$$\frac{1}{k_d}\tan(k_d L_x) + \frac{1}{k_{\text{air}}}[\tan(k_{\text{air}} L_{x2}) + \tan(k_{\text{air}} L_{x1})] - \frac{k_d}{k_{\text{air}}^2}\tan(k_{\text{air}} L_{x1})\tan(k_{\text{air}} L_{x2})\tan(k_d L_x) = 0, \tag{6}$$

$$k_d = \sqrt{\varepsilon_d k_0^2 - \gamma_i^2}, \tag{6a}$$

$$k_{\text{air}} = \sqrt{k_0^2 - \gamma_i^2}, \tag{6b}$$

where k_d, k_{air} is the transverse wavenumber inside the dielectric and air regions shown in the inset of figure 1(a). From these expressions, the value of γ_i is retrieved and from it and applying (4) we obtain $\varepsilon_{\text{eff},i}$. Note that the previous equations converge to the homogenously filled waveguide in the limit when $L_{x1,2} = 0$ and $L_x = b$.

Regarding the characteristic impedance, it can be calculated as follows:

$$Z_i = \frac{\eta_0}{\sqrt{\varepsilon_{\text{eff},i}}} \frac{a}{b} \Delta_a, \tag{7}$$

where $\eta_0 = 120\pi$ (ohm) is the free-space intrinsic impedance. In the previous equation $\Delta_a = 1$ for the input and output waveguides and the transition region of the channel and $\Delta_a \ll 1$ for the ENZ channel.

Putting all together, the transmission coefficient of the sensor is easily obtained [48]:

$$T(f) = \frac{2}{A_{\text{total}} + B_{\text{total}}/Z_{wg} + C_{\text{total}} Z_{wg} + D_{\text{total}}}, \tag{8}$$

where Z_{wg} is the characteristic impedance of the input/output waveguides.

Note that in the equivalent transmission line problem shown in figure 1(b), we have not taken into account the shunt capacitive reactance elements due to the evanescent modes excited at the abrupt interface between the transition region of the channel and ENZ channel, as in [25]. From (7), under the ENZ approximation the effective permittivity is close to zero so that in general $\sqrt{\varepsilon_{\text{eff},I}} \ll \Delta_a$. This implies that the magnitude of the characteristic impedance is very high and hence, the elimination of the shunt capacitances does not strongly affect the performance in the ENZ peak (although it does affect the FP resonance peaks, as discussed below).

In the following section, we analyze several configurations to grasp the performance of the ENZ sensing platform. Analytical results obtained using the transmission line method are compared with simulation results performed with the frequency solver of the commercial simulator CST Microwave Studio®. The metallic walls of all the waveguides of the sensor are assumed to be perfect electric conductors (PEC). Finally, two waveguide ports are used at the input/output of the sensor in order to calculate the transmission coefficient using the S parameters (S_{21}).

3. Results and discussion

In this section, the performance of the ENZ sensor is evaluated for different configurations of the analyte sample. The dimension b is selected as 101.6 mm. The input and output waveguides are filled with a homogeneous dielectric with relative permittivity $\varepsilon_{wg} = 2$, whereas the ENZ channel is filled with air and has a length $L = 1.5b$. Hence, the cutoff frequency is ~1.044 GHz for the input/output waveguides and ~1.476 GHz for the ENZ channel. In the forthcoming studies, all results are normalized to the cutoff frequency of the ENZ channel.

4. Analyte filling the transverse axis

To begin with the analysis, we first study the case of [47] where the analyte fills totally the transverse axis as shown in the inset of figure 2(c). For the calculations, the following parameters are defined: $L_x = b$, $L_z = 0.15b$ ($= 0.1\ L$), $\varepsilon_a = 3$, $\Delta_a = (1/64)$. In figures 2(a), (b) we show the analytical and numerical results of the transmission coefficient versus analyte position and normalized frequency, $\Delta_z \in [-1, 1]$ and $f \in [0.7, 1.3]$, showing good agreement between them. The first transmission peak corresponds to ENZ operation and the second peak is due to a half-wavelength Fabry–Perot (FP) resonance, with a field distribution similar to those shown in figures 2(d), (e), which correspond to an empty channel. A good agreement between analytical and numerical results is observed at the ENZ frequency (first peak) with a larger deviation for the FP peak. The disagreement between the numerical and analytical results in the FP band is a consequence of having disregarded the shunt capacitive reactances at the interface between input/output waveguides and the ENZ channel. Nevertheless, our interest is in the ENZ band which has a negligible deviation. Hence, we will not take into account the capacitance in the following calculations for simplicity without incurring in a large error.

As observed in figures 2(a) and (b), the ENZ band experiences a slight frequency shift as Δ_z is varied, whereas the shift is more notable for the FP band. This distinct behavior is due to the different field distribution of each band. For the ENZ band the field is almost uniform along the channel, whereas at the FP resonance it presents a minimum exactly at the center with maxima at the extremes. Thus, in the latter case the peak position depends strongly on the analyte position. This is in contrast to what happens at the ENZ band which is very robust with respect to a change in Δ_z.

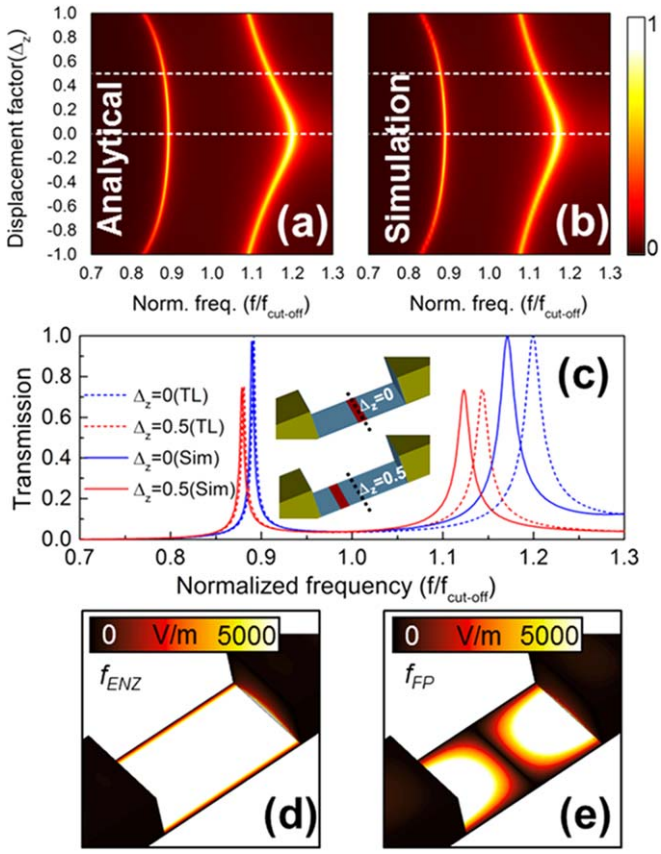

Figure 2. Analytical (a) and numerical (b) results of the transmission coefficient when an analyte slab with $\varepsilon_a = 3$ filling the x axis is shifted along z with a displacement factor from $\Delta_z = -1$ to $\Delta_z = 1$. (c) Analytical (dashed lines) and numerical (solid lines) results of the transmission coefficient for the cases highlighted with dashed lines in (a), (b). Numerical results of the magnitude of the electric field at the ENZ (d) and FP (e) resonances (corresponding to an empty channel).

To better understand the features of each resonance, we select two different z positions of the analyte, $\Delta_z = 0$ and $\Delta_z = 0.5$ (white lines in figures 2(a), (b)) and show the transmission coefficient in figure 2(c). From these results we observe that the agreement is worse for the FP band and that the ENZ band experiences a small downshift ~1.256% from 0.89 ($\Delta_z = 0$) to 0.88 ($\Delta_z = 0.5$), and the amplitude decreases moderately in the last case.

A remarkable point is that in both cases the ENZ peak takes place below the cutoff frequency of the input/output ENZ channels filled with air ($f_{c,ch1} = f_{c,ch2} = 1$, recall that the results are normalized to this frequency) and above the cutoff of the analyte section ($f_{c,a} = 0.57$). This indicates a tunneling of energy through the channels filled with air. Fortunately, this tunneling can be easily explained in impedance terms using the transmission-line model as discussed next.

For simplicity, let us consider the symmetric case when $\Delta_z = 0$ (see the equivalent transmission line problem in figure 3(a)). From (5) we find that the effective permittivity of the air channel sections is negative, as they operate below cutoff. This implies that the propagation constant (4) and the characteristic impedance (7) are imaginary, respectively. Also, note that an aperture on a metallic plane operating below cutoff usually has an inductive character. This is so because the fundamental mode is normally TE that accumulates magnetic energy below cutoff [50]. This means that the characteristic impedance is inductive. With these conditions and provided that the air channel is not too long, the imaginary component of input impedance looking from the analyte section towards the output waveguide [$Z_{\text{in},1}$, black curve in figure 3(b)] has an inductive character. Note that the same impedance appears looking from the analyte towards the input waveguide, given that the structure is symmetric, $Z_{\text{in},3} = Z_{\text{in},1}$.

Next, we calculate the input impedance including the analyte section $Z_{\text{in},2}$ (red curve in figure 3(b)) [48]. It is calculated at the location and direction shown in figure 3(a) as red arrow i.e. the $Z_{\text{in},2}$ is calculated looking to the right of the transmission lines from the location of the analyte. Based on this, $Z_{\text{in},2}$ can be expressed as:

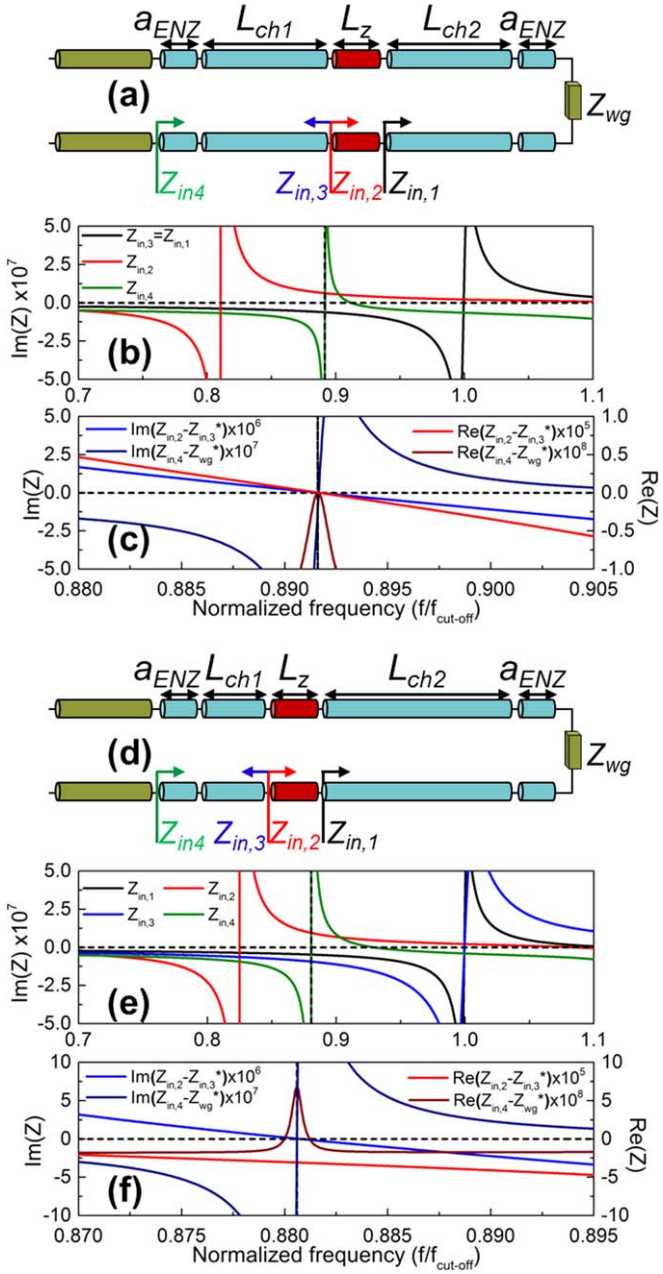

Figure 3. Schematic representation of the equivalent transmission line when the analyte of figure 2 is placed at $\Delta_z = 0$ (a) and $\Delta_z = 0.5$ (d). Analytical results of the imaginary part of the impedances $Z_{\text{in},1}$ (black lines), $Z_{\text{in},2}$ (red lines) $Z_{\text{in},3}$ (blue lines) and $Z_{\text{in},4}$ (green lines) when the analyte is placed at $\Delta_z = 0$ (b) and $\Delta_z = 0.5$ (e). Analytical results of the imaginary (blue lines) and real part (red lines) of the difference between the impedances $Z_{\text{in},2} - Z^*_{\text{in},3}$ (light curves) and $Z_{\text{in},4} - Z^*_{wg}$ (dark curves) for a displacement factor of $\Delta_z = 0$ (c) and $\Delta_z = 0.5$ (f).

$$Z_{\text{in},2} = Z_a \frac{Z_{\text{in},1} + Z_a \tanh(-i\gamma_a L_z)}{Z_a + Z_{\text{in},1} \tanh(-i\gamma_a L_z)}, \tag{9}$$

where Z_a, γ_a is the characteristic impedance and propagation constant at the analyte section. In this case we find that its imaginary part is also inductive for low frequencies but there is a resonance frequency where it diverges and changes its character from inductive to capacitive. This resonance frequency arises due to the denominator of $Z_{\text{in},2}$, which depends on Z_a, γ_a and $Z_{\text{in},1}$. Therefore, since γ_a also changes from imaginary to real (as explained before using equation (5) for the air channel regions) when working below and above cutoff, the imaginary component of $Z_{\text{in},2}$ can change its character from inductive to capacitive.

In equation (9) $Z_a = R_a$ (purely real), $Z_{\text{in},1} \approx -\text{i}\omega L$ (inductive with a negligible real part) and $\gamma_a = \beta_a$ (the analyte section is above cutoff). Therefore, with the prescribed conditions, the denominator of (9) becomes $R_a - \omega L \tan(\beta_a L_z)$ and from here it is obvious that there is a frequency where (9) diverges and the impedance changes from inductive to capacitive. Therefore, at the interface between the channel 1 and the analyte, the impedance looking towards the output ($Z_{\text{in},2}$) is capacitive and looking towards the input ($Z_{\text{in},3}$) is inductive. As

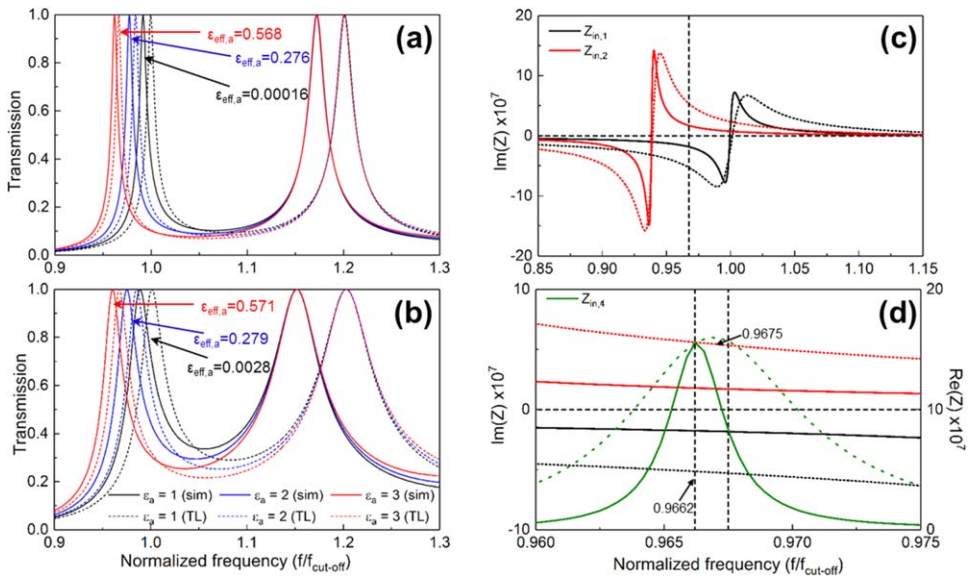

Figure 4. Analytical (dashed lines) and numerical (solid lines) results of the transmission coefficient when an analyte with transversal dimensions $L_x = L_z = 0.1\ L = 0.15b$ and relative permittivity $\varepsilon_a = 1$ (black), $\varepsilon_a = 2$ (blue) and $\varepsilon_a = 3$ (red) is placed in the middle of the channel with height $a_{\mathrm{ENZ}} = (1/64)a$ (a) and $a_{\mathrm{ENZ}} = (1/20)a$ (b). The effective permittivity ($\varepsilon_{\mathrm{eff},a}$) calculated using (5) and (6) is also shown in panels (a), (b) where almost the same values are obtained for both heights of the channel. (c) Analytical results of the imaginary part of the impedances $Z_{\mathrm{in},1}$ (black lines), $Z_{\mathrm{in},2}$ (red lines) when the analyte with the same dimensions as (a), (b) and $\varepsilon_a = 3$ is placed within a narrow channel with height $a_{\mathrm{ENZ}} = (1/64)a$ (solid lines) and $a_{\mathrm{ENZ}} = (1/20)a$ (dotted lines). (d) Zoom-in of the results shown in panel (c) along with the real part of $Z_{\mathrm{in},4}$ (green lines). The vertical/horizontal black dashed lines correspond to the ENZ frequency shown in panels (a), (b) and to the points where the imaginary part of the impedance is equal to zero, respectively.

it is shown in figure 3(b), the capacitive reactance of $Z_{\mathrm{in},2}$ is reduced for higher frequencies while the inductive reactance $Z_{\mathrm{in},3}$ increases. Thus, there is a frequency where both cancel (i.e. they are exactly complex conjugated) giving rise to the peak of transmission shown in figure 2(c). We have plotted $Z_{\mathrm{in},2} - Z^*_{\mathrm{in},3}$ in figure 3(c). As shown both real and imaginary components cross zero at the frequency of the ENZ peak (marked as vertical dashed line). Hence we have maximum transmission at this frequency. For the sake of completeness we have depicted in the same figures the impedance difference at the input, $Z_{\mathrm{in},4} - Z_{wg}$ and we find that there is impedance matching exactly at the peak of transmission.

When the analyte is shifted to $\Delta_z = 0.5$ the impedances suffer a slight modification (see the equivalent transmission line in figure 3(d)) and the peak of transmission downshifts and its amplitude is reduced (see figure 2(c)). This performance can be also explained by analyzing this case using the transmission line impedances. The results of the imaginary part of $Z_{\mathrm{in},1}$, $Z_{\mathrm{in},2}$ and $Z_{\mathrm{in},3}$ and $Z_{\mathrm{in},4}$ for this configuration are shown in figure 3(e). The performance is similar to the previous case. The peak of transmission ($f = 0.8807$) happens when the $\mathrm{Im}\{Z_{\mathrm{in},2}\} = -\mathrm{Im}\{Z_{\mathrm{in},3}\}$. However, due to the asymmetry of the problem at this condition $\mathrm{Re}\{Z_{\mathrm{in},2}\} \neq \mathrm{Re}\{Z_{\mathrm{in},3}\}$ as shown in figure 3(f), so the impedances are not conjugate matched. Likewise, $\mathrm{Re}\{Z_{\mathrm{in},4}\} \neq \mathrm{Re}\{Z_{wg}\}$ and therefore the peak of transmission does not reach unity. From this analysis it is clear that the transmission line model is very powerful to explain even the most peculiar details of the spectrum.

5. General case

Now we analyze the general case when the analyte does not completely fill neither the transversal nor the longitudinal dimension. The study is done for different sizes, permittivity values and positions of the analyte. First we consider the case in which the analyte has a square cross-section on the *xz*-plane with transversal dimensions $L_x = L_z = 0.15b$ and permittivity (ε_a) varying from 1 to 3 placed at $\Delta_x = \Delta_z = 0$. Two different channel heights are evaluated $\Delta_a = (1/64)$ and $\Delta_a = (1/20)$. The analytical and numerical results of the transmission coefficient are shown in figure 4.

By inspection of figure 4 it is observed that an increment of the analyte permittivity ε_d provokes a noticeable redshift of the ENZ band. From equation (6), increasing ε_d implies an increment of the propagation constant at the analyte section, $\gamma_{\mathrm{eff},a}$, and also from equation (5) an increment of the effective permittivity, $\varepsilon_{\mathrm{eff},a}$. At the same time, the characteristic impedance, Z_a, decreases, see (7). All these conditions together make the denominator of (9) diverge at a smaller frequency as ε_d is augmented, producing a redshift of the ENZ peak. On the other hand,

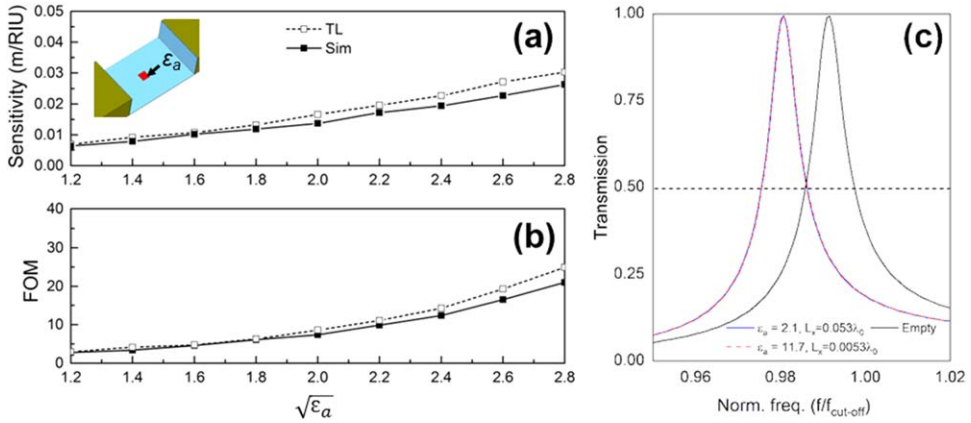

Figure 5. Sensitivity (a) and FOM (b) results for an analyte of dimensions $L_x = L_z = 0.1\ L = 0.15b$ inside an ENZ channel of height $a_{\mathrm{ENZ}} = (1/64)a$. (c) the transmission spectra for the smallest dielectric analyte detectable, with $L_x = 0.053\lambda_0$ and $L_x = 0.0053\lambda_0$ using a permittivity of the analyte of $\varepsilon_a = 2.1$ (Teflon) and $\varepsilon_a = 11.7$ (Silicon), respectively. The black dashed line in the inset shows the value of transmission of 0.5 where the spectra of both analytes intercept the spectrum of the empty channel.

the FP band remains the same. This is because at the FP resonance has a minimum field intensity at $\Delta_z = 0$ so the electric field barely interacts with the analyte and therefore it is insensitive to a change in permittivity.

By comparing the cases $\Delta_a = (1/64)$ and $\Delta_a = (1/20)$ it can be concluded that reducing the channel height produces an enhancement of the quality factor of the peaks, both for the ENZ and FP bands. This performance was explained in [47] where it was argued that for extremely narrow channels the impedance matching bandwidth of the ENZ channel becomes more and more restrictive. It can be also explained following the same reasoning, as in the previous section. The characteristic impedance of the transmission lines is directly proportional to the factor Δ_a, see (7). Therefore, for small Δ_a the characteristic impedance is very small. From here it is clear that at any frequency (with the exception of resonance peaks) the magnitude of the impedances $Z_{\mathrm{in},1}, Z_{\mathrm{in},2}$ decrease for small Δ_a, as demonstrated in figures 4(c), (d), which corresponds to the case $\varepsilon_a = 3$. Note that the ENZ frequency is slightly blue shifted from 0.9662 to 0.9675 when $\Delta_a = (1/64)$ and $\Delta_a = (1/20)$, respectively. This blue shifting can also be observed in figures 4(a), (b) where the effective permittivity for each case is shown. This happens because the length of the walls used in the U-channel changes when modifying Δ_a (see figure 1). However, since the height of the channel and the length of the walls are still ultra-narrow for both cases, the frequency shifting represents only ~0.14%. In the figure, it is clearly shown that the impedance matching bandwidth is less restrictive for $\Delta_a = (1/20)$. Thus, there are more frequencies around the ENZ frequency where the inductive and capacitive reactances of $Z_{\mathrm{in},1}$ and $Z_{\mathrm{in},2}$ are approximately complex conjugated. This produces a reduction of the Q factor and a widening of the peak of transmission around the ENZ frequency.

As demonstrated in figures 4(a), (b), an interesting feature of this sensor is that it is still possible to detect a change of permittivity at the ENZ peak, even with extremely small analytes ($L_x = L_z = 0.075\lambda_0$, as in this case). Generally, the performance of a sensor is given by the sensitivity, S, and the figure of merit, FoM. The sensitivity is defined as the variation of the resonance wavelength divided by the variation of the index refraction, $S = \Delta\lambda_{\mathrm{res}}/\Delta n$ [m/RIU], where RIU stands for refractive index unit [51, 52]. In our case, the sensitivity is given by the redshift of the ENZ peak when the refractive index of the analyte varies. In sensing applications, besides a high S, a good selectivity (i.e. spectral resolution) is usually desired. Then, high Q-factor resonances, or equivalently, narrow full width at half maximum (FWHM) values are preferred. The FOM relates both parameters: FOM $= S/$FWHM [dimensionless]. In figures 5(a), (c), both analytical and simulation results of the S and FOM are shown, with a good agreement between them. A maximum S of 0.028 and 0.03 m/RIU is obtained in the simulation and analytical results, respectively. What is more, very competitive FOM values are obtained [53] (up to 21 and 25 from the simulation and analytical results, respectively), due mainly to the strongly sharp response of the ENZ peak. For the sake of completeness, the transmission spectra for an analyte with $L_x = 0.053\lambda_0$ and $L_x = 0.0053\lambda_0$ using Teflon ($\varepsilon_{\mathrm{d}} = 2.1$) and Silicon ($\varepsilon_{\mathrm{d}} = 11.7$) are shown in figures 5(c) along with the transmission spectrum of an empty channel. The L_x dimension of the analytes correspond to the limiting case where the ENZ peak of the loaded and unloaded (i.e. empty) structure cross at 0.5 (FWHM). This indicates the smallest analyte dimension detectable with the proposed sensor. From these results it can be corroborated how the ENZ sensor is able to detect the frequency shift of the ENZ peak due to the presence of extremely subwavelength dielectric bodies.

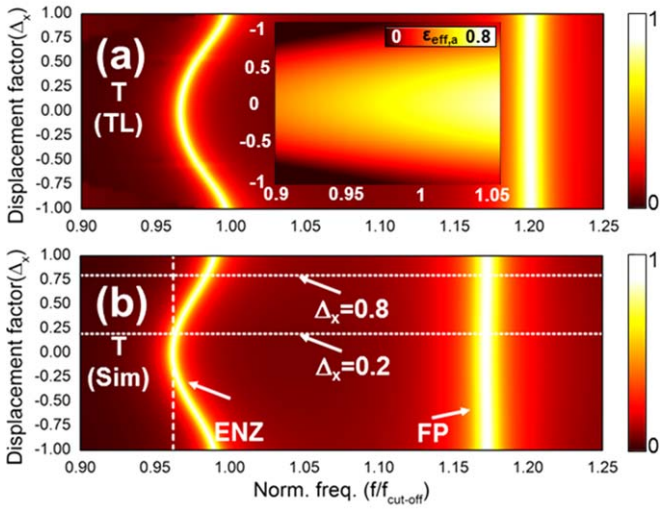

Figure 6. Analytical (a) and numerical (b) results of the transmission coefficient for an analyte with relative permittivity $\varepsilon_a = 3$ placed at $\Delta_z = 0$ with dimensions $L_x = L_z = 0.1$ $L = 0.5b$ as a function of the displacement factor $\Delta_x \in [-1, 1]$ and the normalized frequency. (Inset) analytical values of the effective permittivity ($\varepsilon_{\text{eff},a}$) for the same configuration as in panel a.

6. Changing the position of the analyte

Next, we study the sensing performance when the position of the analyte is changed. The analytical and numerical results of the transmission coefficient as a function of the normalized frequency and Δ_x for a dielectric particle with $\varepsilon_a = 3$ and dimensions $L_x = L_z = 0.1$ $L = 0.15b$ placed at $\Delta_z = 0$, are shown in figure 6. A good agreement between numerical and analytical results is observed at the ENZ frequency with some deviation at the FP resonance, as expected.

When $\Delta_x = 0$ the ENZ peak takes place at $f = 0.963$ and shifts to $f = 0.997$ for $\Delta_x = \pm 1$. Expectedly, near the walls the electric field of the fundamental mode TE_{10} vanishes and therefore the interaction between the analyte and the electric field is very small, making the ENZ frequency approach the value of an empty channel. Conversely, the electric field magnitude at the center is maximum causing the largest frequency shift. For the sake of completeness the effective permittivity ($\varepsilon_{\text{eff},a}$) calculated using (5) and (6) within the frequency range of the ENZ frequency is shown in the inset of figure 6(a). Again, when the analyte is near the edges, $\varepsilon_{\text{eff},a}$ approaches zero at lower frequencies. In contrast, $\varepsilon_{\text{eff},a}$ increases as the analyte is shifted towards the center, demonstrating an enhanced interaction between the electric field and the analyte. As for the FP peak, it is observed that it does not shift with Δ_x, since at $\Delta_z = 0$ the electric field has a minimum for this resonance, as it has been explained in figures 2(d), (e).

The results of transmission coefficient at the ENZ frequency (dashed vertical lines in figure 6) are shown in figure 7(a), as a function of Δ_x along with the values of $\varepsilon_{\text{eff},a}$. In this figure, the influence of the analyte position on the performance of the ENZ sensor is evident. Moreover, the transmission coefficient for $\Delta_x = 0.2$ and $\Delta_x = 0.8$ (taken from the horizontal lines in figure 6) are shown in figure 7(b) where it is clearly shown that the frequency shifting depends on the position of the analyte.

To further analyze this performance, the same study shown in figure 6 was carried out considering a different permittivity of the analyte ($\varepsilon_d = 2$). The results of the cutoff frequency within the analyte region at different positions along the x axis are shown in figure 7(c) for both analytes ($\varepsilon_d = 2$ and $\varepsilon_d = 3$). From this figure, it is clearly observed how the cutoff frequency is closer to 1 when the analyte is closer to the lateral metallic walls, as discussed before. For the sake of completeness, the transmission coefficient for the same locations along the x axis for both analytes is shown in figure 7(d) calculated at their corresponding ENZ frequency when $\Delta_x = \pm 1$. As observed, the transmission coefficient is reduced when the analyte is moved closer to the center, as expected, due to the fact that the ENZ peak is shifted to lower frequencies (as seen in figure 7(c)). It is important to note that here we have limited the study to the case where the analyte is completely covering the ENZ-channel along the y axis. However, similarly to the studies shown before for the analyte at different locations along the x axis, if an analyte with $L_y < a_{\text{ENZ}}$ is used the ENZ transmission peak will be moved closer to the ENZ frequency of the empty channel. This is due to the fact that the smaller the analyte the lower the interaction with the incoming electric field of the TE_{10} mode.

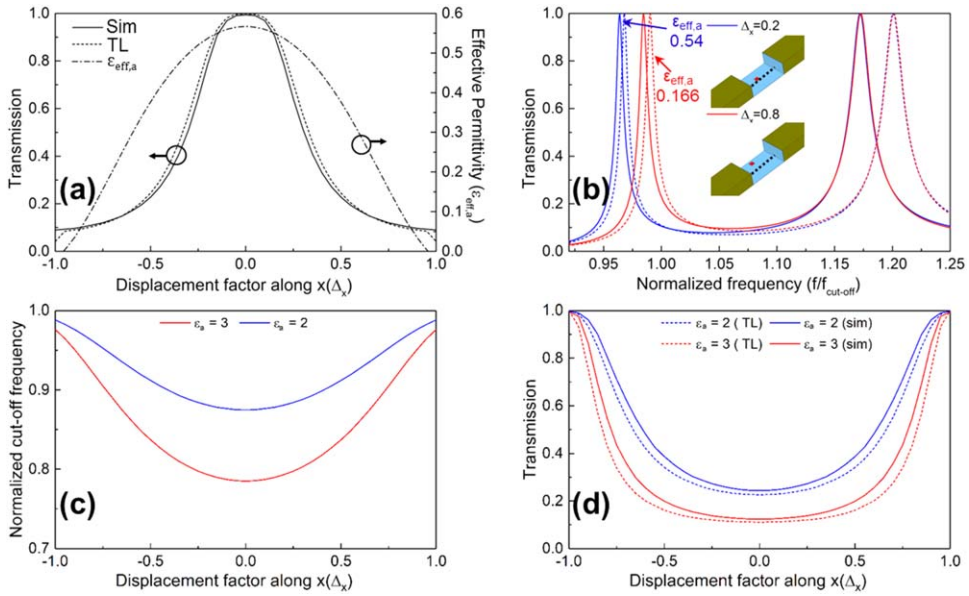

Figure 7. (a) Analytical (dashed line) and numerical (solid line) results of the transmission coefficient along with the analytical values of the effective permittivity $\varepsilon_{\text{eff},a}$ (dashed–dotted line) as a function of Δ_x at the ENZ frequency (results taken from the vertical lines shown in figure 6). (b) Numerical (solid lines) and analytical (dashed lines) results of the transmission coefficient for an analyte with $L_x = 0.1$ $L = 015b$, and $\Delta_x = 0.2$ (blue lines), $\Delta_x = 0.8$ (red lines) (results taken from the horizontal lines shown in figure 6). Cutoff frequency within the analyte region (c) and transmission coefficient (d) when the analyte [with the same dimensions as panels (a) and (b)] is moved along the x axis considering a permittivity of the analyte of $\varepsilon_a = 2$ (blue lines) and $\varepsilon_a = 3$ (red lines). The analytical and numerical results are plotted as solid and dashed lines, respectively. In panel (d), the transmission coefficient at different positions is calculated at the ENZ frequency when the analyte moved along the x axis.

7. Effective medium evaluation

Now we evaluate the sensing performance when the cross-section of figure 1(a) is treated as an effective medium with a permittivity $\varepsilon_{\text{eff},a}$. Consider that a dielectric analyte with $\varepsilon_a = 3$, $L_x = 0.3b$ and $L_z = 0.15b$ is placed at $\Delta_z = 0$ and $\Delta_x = 0.5$, as shown in the inset of figure 8(a). From the transmission results of figure 8(a), and applying (5) and (6), we find that the effective permittivity of the analyte cross-section is $\varepsilon_{\text{eff},a} = 0.8883$ at the ENZ peak ($f = 0.95$). However, this is not the only possibility to obtain this effective permittivity. In fact, there are infinite combinations of size, position and permittivity of the analyte that lead exactly to the same $\varepsilon_{\text{eff},a}$. In the forthcoming, we will demonstrate that the transmission coefficient can be uniquely described by this effective permittivity value, giving exactly the same spectral performance, provided that we are always working at the same Δ_z (we saw in figure 2 that a change of Δ_z implies a modification of the sensor response) and keep the same value for L_z.

First, we keep the same dimensions but place the analyte at $\Delta_x = \Delta_z = 0$, as shown in the inset of figure 8(b). We can tune the permittivity to get the same effective permittivity ($\varepsilon_{\text{eff},a} = 0.8883$) at the ENZ frequency (0.95). After the calculation, we get $\varepsilon_a = 2.697$. Note that this value is smaller than before, as expected, since the interaction of the analyte with the electric field increases when it is placed at the center, so a smaller permittivity is necessary to have the same response. The transmission coefficient for this configuration is depicted in figure 8(b), showing a good agreement with the previous case.

In addition, we can also modify the width of the analyte, instead of its permittivity. Using the same procedure we obtain $L_x = 0.2439b$, which is expectedly smaller than the initial case. The transmission coefficient for this case is shown in figure 8(c), where a good agreement is again observed. Finally, we can consider that the analyte fills completely the x-axis and tune its permittivity. After applying the same procedure as before the calculated value is $\varepsilon_a = 2.0029$, which is smaller than the magnitude of figures 8(a), (b), as expected. The transmission coefficient for this case is shown in figure 8(d) with a good agreement with the previous cases. By comparing all the cases, it can be observed that the agreement is not only at the ENZ frequency but within the entire spectrum. This is due to the dispersive performance of the waveguide, even when the parameters of the analyte have been calculated at a single frequency. Hence, it is only necessary to calculate the permittivity at a single frequency and then we will obtain the same response for all the frequencies. Note that this performance is only valid provided the analyte is not dispersive (which is the most usual case, at least within a limited bandwidth) and it has $\varepsilon_d > 1$. These results demonstrate that the response of different configurations is identical if they can be reduced to the same effective permittivity.

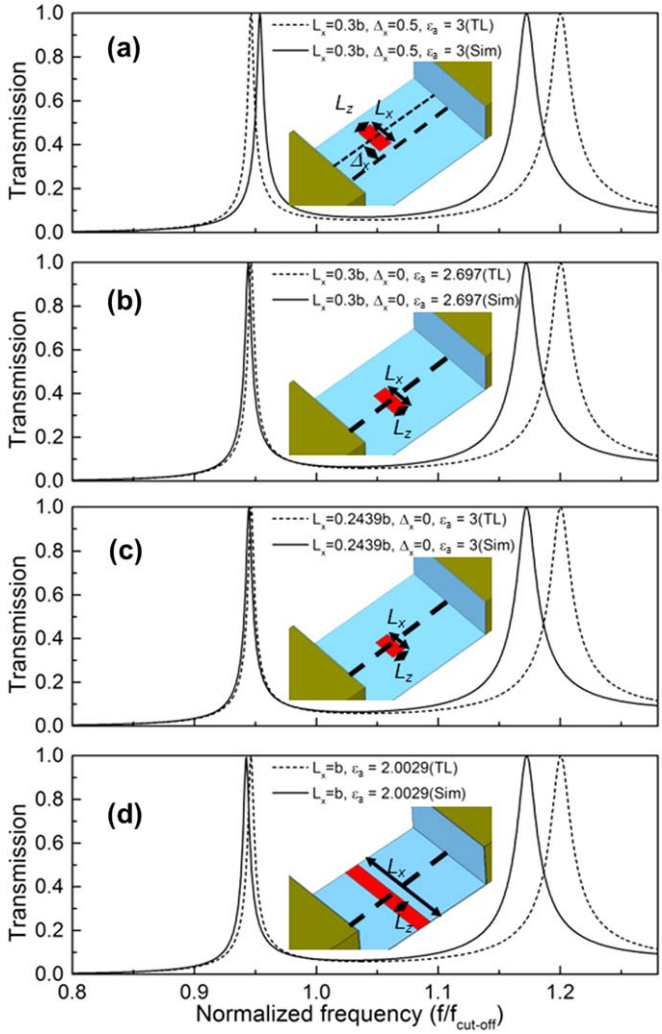

Figure 8. Analytical (dashed lines) and numerical (solid lines) results of the transmission coefficient for different configurations of the analyte inside of the ENZ channel synthetized using the effective permittivity approach: (a) a dielectric analyte shifted at $\Delta_x = 0.5$ with lateral dimensions $L_x = 0.3b$ and $\varepsilon_a = 3$, (b) a dielectric analyte at $\Delta_x = 0$ with the same dimensions but $\varepsilon_a = 2.697$, (c) a dielectric analyte at $\Delta_x = 0$ with lateral dimensions $L_x = 0.2439b$ and $\varepsilon_a = 3$ and (d) a dielectric analyte completely filling the transversal axis with and $\varepsilon_a = 2.0029$. $L_z = 0.15b$ in all cases.

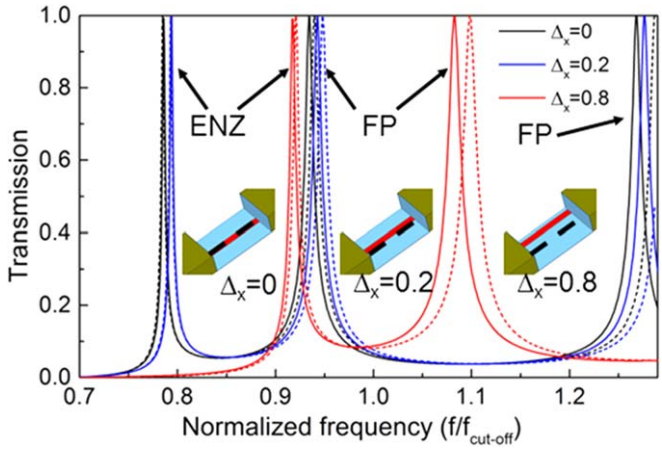

Figure 9. Analytical (dashed lines) and numerical (solid lines) results of the transmission coefficient of an analyte with $\varepsilon_a = 3$, $L_x = 0.1$ $L = 0.5b$ and $L_z = L$ moved along the transversal x-axis with a displacement factor $\Delta_x = 0$ (black lines), $\Delta_x = 0.2$ (blue lines) and $\Delta_x = 0.8$(red lines).

8. Dielectric cavity completely filling the transversal *z*- axis

As a final step, we also study the performance of the sensor considering that now the analyte fills completely the propagation *z*-axis ($L_z = L$), keeping the same permittivity $\varepsilon_a = 3$ and width $L_x = 0.1\ L = 0.5b$. The numerical and analytical results of the transmission coefficient at three different positions, $\Delta_x = 0$, $\Delta_x = 0.2$ and $\Delta_x = 0.8$, are shown in figure 9 (see the insets to better discern each position). From these results, three peaks of transmission are clearly observed: one due to the ENZ frequency and two related to FP resonances. This larger number of peaks is due to the increase of the effective permittivity of the narrow ENZ channel, which shifts the spectrum towards lower frequencies so that more resonances can be excited within the same length (L). The transmission peaks are moved to higher frequencies as Δ_x increases, with a similar performance for the case of a dielectric particle. The main difference with the results shown in figure 4 is that now all the peaks are shifted. In the present configuration, the analyte covers completely the *z* axis enhancing the interaction with electric field, whereas in the previous case it was limited to the center, where the field has a minimum. Moreover, for the case shown in figure 9, the whole narrow ENZ channel could be modeled as a channel filled with an effective permittivity (as described in the previous section), which will produce a shift of all the excited peaks.

9. Conclusions

A systematic study of the sensing performance of an ENZ-based sensor has been presented using analytical techniques and numerical simulations. A transmission-line model has been derived to study the performance of the sensor with excellent agreement with numerical simulations in all the scenarios considered. It has been found that when an analyte with relative permittivity larger than unity is inserted in the channel, the ENZ peak takes place below cutoff of the channels filled with air. This result has been comprehensively explained using the transmission-line model and it has been found that it is due to complex conjugate matching with the inductive impedance of the waveguides below cutoff. A homogenization model for the case where the analyte does not completely fill either the transversal or the propagation axis has been successfully implemented. An excellent performance of the sensing platform has been demonstrated even with very small analyte sizes ($\sim 0.05\lambda_0$). Competitive values for both sensitivity (up to 0.03 m/RIU) and FoM (about 25) have been obtained. It has been shown that the position of the analyte along the *x*-axis is an important parameter, since the interaction with electric field is maximum at the center and vanishes at the sides, as corresponds to the fundamental TE_{10} mode. On the other hand, it has been shown that ENZ peak has a robust performance in terms of the position of the analyte along the *z*-axis. Hence, a better performance is achieved at the ENZ frequency compared with the results at the FP resonance. These results show that this type of structures are promising for future sensing platforms based on ENZ resonance. An experimental demonstration of the theory presented here is expected to be developed in the near future.

Acknowledgments

VP-P is supported by the Newcastle University (Newcastle University Research Fellow). MB acknowledges support by the Spanish Ministerio de Economía y Competitividad under contract TEC2014-51902-C2-2-R. PR-U was sponsored by Public University of Navarra via a predoctoral scholarship. NE acknowledges the partial support from the Vannevar Bush Faculty Fellowship program sponsored by the Basic Research Office of the Assistant Secretary of Defense for Research and Engineering and funded by the Office of Naval Research through grant N00014-16-1-2029.

ORCID iDs

V Pacheco-Peña https://orcid.org/0000-0003-2373-7796
M Beruete https://orcid.org/0000-0001-8370-0034
N Engheta https://orcid.org/0000-0003-3219-9520

References

[1] Marqués R, Martín F and Sorolla M 2008 *Metamaterials with Negative Parameters: Theory, Design and Microwave Applications* (Hoboken. NJ: Wiley)
[2] Pendry J B 2000 *Phys. Rev. Lett.* **85** 3966
[3] Smith D R, Padilla W J, Vier D C, Nemat-Nasser S C and Schultz S 2000 *Phys. Rev. Lett.* **84** 4184
[4] Lier E, Werner D H, Scarborough C P, Wu Q and Bossard J A 2011 *Nat. Mater.* **10** 216

[5] Zheludev N I and Kivshar Y S 2012 *Nat. Mater.* **11** 917
[6] Poddubny A, Iorsh I, Belov P and Kivshar Y 2013 *Nat. Photon.* **7** 948
[7] Neu J, Beigang R and Rahm M 2013 *Appl. Phys. Lett.* **103** 041109
[8] Pacheco-Peña V, Navarro-Cía M, Orazbayev B, Minin I V, Minin O V and Beruete M 2015 *IEEE Trans. Antennas Propag.* **63** 3710
[9] Li A Y, Kita S, Muñoz P, Reshef O, Vulis D I, Yin M, Loncar M and Mazur E 2015 *Nat. Photon.* **9** 738
[10] Pacheco-Peña V, Orazbayev B, Torres V, Beruete M and Navarro-CÍa M 2013 *Appl. Phys. Lett.* **103** 183507
[11] Pacheco-Peña V, Minin I V, Minin O and Beruete M 2017 *IEEE Antennas Wirel. Propag. Lett.* **16** 1460
[12] Elek F and Eleftheriades G V 2005 *New J. Phys.* **7** 163
[13] Prudêncio F R, Costa J R, Fernandes C A and Engheta N 2017 *New J. Phys.* **9** 123017
[14] Shelby R A, Smith D R and Schultz S 2001 *Science* **292** 77
[15] Enoch S, Tayeb G, Sabouroux P, Guerin N and Vincent P 2002 *Phys. Rev. Lett.* **89** 213902
[16] Smith D, Rye P, Mock J, Vier D and Starr A 2004 *Phys. Rev. Lett.* **93** 137405
[17] Engheta N and Ziolkowski R 2006 *Metamaterials: Physics and Engineering Explorations* (Hoboken, NJ: Wiley)
[18] Dolling G, Enkrich C, Wegener M, Soukoulis C M and Linden S 2006 *Science* **312** 892
[19] Solymar L and Shamonina E 2009 *Waves in Metamaterials* (Oxford: Oxford University Press)
[20] Paul O, Reinhard B, Krolla B, Beigang R and Rahm M 2010 *Appl. Phys. Lett.* **96** 241110
[21] Demetriadou A and Hao Y 2011 *IEEE Antennas Wirel. Propag. Lett.* **10** 1590
[22] Garcia N, Ponizovskaya E V and Xiao J Q 2002 *Appl. Phys. Lett.* **80** 1120
[23] Silveirinha M and Engheta N 2006 *Phys. Rev. Lett.* **97** 157403
[24] Silveirinha M G and Engheta N 2007 *Phys. Rev.* B **76** 245109
[25] Alù A, Silveirinha M G and Engheta N 2008 *Phys. Rev.* E **78** 016604
[26] Liberal I and Engheta N 2017 *Nat. Photon.* **11** 149
[27] Edwards B, Alù A, Young M E, Silveirinha M and Engheta N 2008 *Phys. Rev. Lett.* **100** 033903
[28] Liu R, Cheng Q, Hand T, Mock J J, Cui T J, Cummer S A and Smith D R 2008 *Phys. Rev. Lett.* **100** 1
[29] Subramania G, Fischer A J and Luk T S 2012 *Appl. Phys. Lett.* **101** 241107
[30] Zhang S, Fan W, Panoiu N C, Malloy K J, Osgood R M and Brueck S R J 2005 *Phys. Rev. Lett.* **95** 137404
[31] Maas R, Parsons J, Engheta N and Polman A 2013 *Nat. Photon.* **7** 907
[32] Engheta N 2007 *Science* **317** 1698
[33] Li Y, Liberal I, Giovampaola C D and Engheta N 2016 *Sci. Adv.* **2** e1501790
[34] Powell D, Alù A, Edwards B, Vakil A, Kivshar Y and Engheta N 2009 *Phys. Rev.* B **79** 245135
[35] Alù A and Engheta N 2010 *IEEE Trans. Antennas Propag.* **58** 328
[36] Soric J C, Engheta N, MacI S and Alu A 2013 *IEEE Trans. Antennas Propag.* **61** 33
[37] Forati E, Member G S, Hanson G W and Sievenpiper D F 2015 *IEEE Trans. Antennas Propag.* **63** 1909
[38] Pacheco-Peña V, Torres V, Orazbayev B, Beruete M, Navarro-Cía M, Sorolla M and Engheta N 2014 *Appl. Phys. Lett.* **105** 243503
[39] Rodríguez-Fortuño F J, Vakil A and Engheta N 2014 *Phys. Rev. Lett.* **112** 033902
[40] Navarro-Cía M, Beruete M, Sorolla M and Engheta N 2012 *Phys. Rev.* B **86** 165130
[41] Alù A, Silveirinha M, Salandrino A and Engheta N 2007 *Phys. Rev.* B **75** 155410
[42] Pacheco-Peña V, Torres V, Beruete M, Navarro-Cía M and Engheta N 2014 *J. Opt.* **16** 094009
[43] Torres V, Orazbayev B, Pacheco-Peña V, Teniente J, Beruete M, Navarro-Cia M, Sorolla M and Engheta N 2015 *IEEE Trans. Antennas Propag.* **63** 231
[44] Pacheco-Peña V, Navarro-Cía M and Beruete M 2016 *Opt. Laser Technol.* **80** 162
[45] Pacheco-Peña V, Engheta N, Kuznetsov S, Gentselev A and Beruete M 2017 *Phys. Rev. Appl.* **8** 034036
[46] Rotman W 1962 *IRE Trans. Antennas Propag.* **10** 82
[47] Alù A and Engheta N 2008 *Phys. Rev.* B **78** 1045102
[48] Pozar D M 1998 *Microwave Engineering* 4th edn (Hoboken, NJ: Wiley)
[49] Torres V, Pacheco-Peña V, Rodríguez-Ulibarri P, Navarro-Cía M, Beruete M, Sorolla M and Engheta N 2013 *Opt. Express* **21** 9156
[50] Colling R E and Zucker F J 1969 *Antenna Theory* (New York: McGraw-Hill)
[51] O'Hara J F, Withayachumnankul W and Al-Naib I 2012 *J. Infrared, Millim., Terahertz Waves* **33** 245
[52] Singh R, Cao W, Al-Naib I, Cong L, Withayachumnankul W and Zhang W 2014 *Appl. Phys. Lett.* **105** 171101
[53] Ng B, Wu J, Hanham S M, Fernández-Domínguez A I, Klein N, Liew Y F, Breese M B H, Hong M and Maier S A 2013 *Adv. Opt. Mater.* **1** 543